Full field cold-formed steel column buckling measurements with high resolution image-based reconstruction

A. Lama Salomon[1], D. Fratamico[2], B.W. Schafer[3], C.D. Moen[4]

Abstract

High resolution optical cameras and computer vision algorithms are employed in this research to create full field digital state models (3D+time) of buckling deformation over the full length of six built-up cold-formed steel column tests, from initial loading to collapse to the post-buckling response. Corresponding buckling and load-deformation response are always of interest in a thin-walled structure experiment because capacity and stiffness degradation can be related to elastic buckling modes that serve as the basis for capacity prediction equations in codes and standards. In a typical experiment, these modes are only coarsely tracked at discrete points with displacement transducers, or they can be measured with accurate laser-based systems down to 0.025 mm (0.001 in.) that typically requires equipment moving along a rail which is challenging to implement many times during an actual experiment.

The image-based reconstruction approach in this research is different because it uses a series of cameras mounted around a cold-formed steel column that are controlled together to take pictures from strategically located vantage points six times per minute over the course of the test. Pixels common to multiple images are identified and relative positions are used to calculate their 3D coordinates in a point cloud, providing a full field time record of the experiment. These digital state models provide valuable information that can be used for buckling mode decomposition and to validate and inspire evolving analysis and design methods for thin-walled structures.

[1] Graduate Research Assistant, Civil & Environmental Engineering, Virginia Tech, <abrah89@vt.edu>
[2] Graduate Research Assistant, Dept. of Civil Engineering, Johns Hopkins University, < fratamico@jhu.edu>
[3] Professor, Dept. of Civil Engineering, Johns Hopkins University, < schafer@jhu.edu>
[4] Associate Professor, Civil & Environmental Engineering, Virginia Tech, <cmoen@vt.edu>

1. Introduction

Digital state models are representations of objects that can be created using a wide variety of methods, which require the interaction between a sensor (e.g., coordinate measuring machines) or a radiation (e.g., sonar) and the object's surface (Bellocchio 2013). Particularly, the creation of 3D models from images (3D image-based reconstruction), taken with off the shelf point-and-click digital still or video cameras, is interesting because of the reduced cost, adaptability and the lack of physical contact measurement tools (e.g. calipers, wire potentiometers, rulers).

Technology to produce accurate state models using image-based reconstruction is already mature (Wu 2011; Wu 2013) and is being used in civil engineering applications such as buckling mode decomposition of cold-formed steel elements (Lama Salomon et al., 2015), infrastructure condition assessment (Lama Salomon et al. 2016; Lattanzi and Miller 2015) and construction management (Golparvar-Fard et al. 2009). 3D data can be built using optical imaging to compute displacement fields, measure initial imperfections or find buckling mode participation factors (Lama Salomon et al. 2015; Cai et al. 2015).

This research presents documentation of structural testing applied to thin-walled cold-formed steel built-up columns in compression, creating a 3D digital state model every 10 seconds during the experiment, including the initial state before loading, capturing geometric imperfections. The digital state models are used to quantify the effect of fastener layout (specifically, self-drilling screws connecting the webs) on the local and distortional buckling and collapse behavior of a series of back-to-back lipped channel sections. These tests follow elastic buckling studies performed on built-up cold-formed steel columns using springs and constraints as fasteners in finite element and finite strip-based models in search of efficient methods of quantifying composite action in compression members (Fratamico and Schafer 2014). The goal of this study is to highlight image-based reconstruction as a useful tool for quantifying complex thin-walled behavior like that observed in built-up members.

2. 3D Image-Based Reconstruction

3D image-based reconstruction estimates the structure of three-dimensional objects using images. Multiple algorithms exists to estimate 3D structures using silhouettes (Potmesil 1987), textures (Blostein and Ahuja 1989; Didden et al. 2015), defocus (Favaro and Soatto 2005) and cameras motion (Torresani et al. 2008). The coordinates (X, Y, Z) of each point in the scene can be computed using triangulation if they are shared by two or more cameras of known location and orientation. Nevertheless, the method implemented in this project (structure from motion) assumes that no information about the cameras' pose is available. Therefore, the structure from motion (SFM) problem results in, given "n" fixed 3D points shared by "m" images, estimate "m" camera poses and "n" 3D points coordinates $S_i = (X_i, Y_i, Z_i)$ from the "mn" corresponding 2D points.

This formulation of the SFM problem turns into the chicken or the egg dilemma, the cameras' pose is needed to compute the 3D point's coordinates and viceversa. However, there is a geometric constraint (epipolar constraint) that allows the computation of the cameras' pose without including the 3D point coordinates in the equations. Fig. 1 illustrate the typical 'pinhole' camera model (where light rays travel along straight lines from the 3D scene onto a camera 2D image plane), the relationship between 3D point coordinates and 2D image coordinates, and the epipolar geometry.
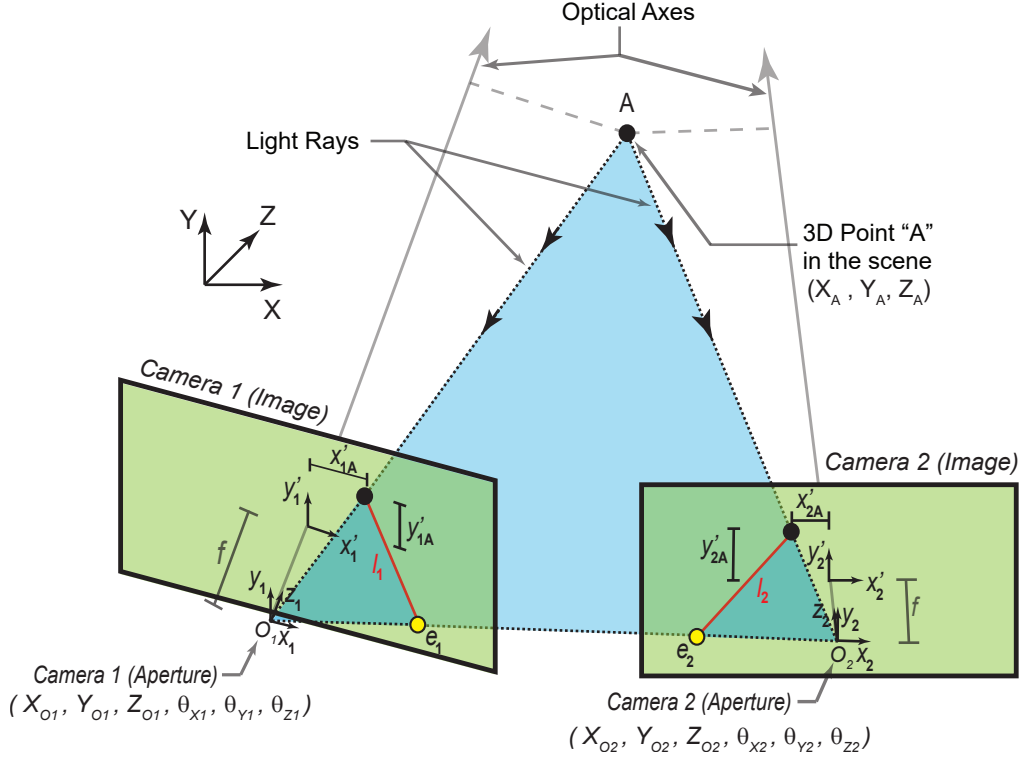
Figure 1. Pinhole camera model, where (X, Y, Z) is the world coordinate frame, (x_i, y_i, z_i) is the local coordinate system for camera i, (x'_i, y'_i) is the 2D image coordinate frame for camera i, O_i is the point of projection (aperture) for camera i, f is the distance from O_i to the center of the image plane (focal length), $(X_{Oi}, Y_{Oi}, Z_{Oi}, \theta_{Xi}, \theta_{Yi}, \theta_{Zi})$ is the camera i pose in the world coordinate system, e_i are the intersections of the line (O_1, O_2) with each image plane (epipoles), and l_1 and l_2 are the intersections between the epipolar plane (O_1, O_2, A) and the image planes.

The 3D coordinates (X, Y, Z) of point j can be mapped into the local coordinates (x_i, y_i, z_i) of camera i using

$$\begin{bmatrix} x_i \\ y_i \\ z_i \end{bmatrix} = \begin{bmatrix} r_{11} & r_{12} & r_{13} & x_t \\ r_{21} & r_{22} & r_{23} & y_t \\ r_{31} & r_{32} & r_{33} & z_t \end{bmatrix} \begin{bmatrix} X \\ Y \\ Z \\ 1 \end{bmatrix} \tag{1}$$

$$\begin{bmatrix} x_i \\ y_i \\ z_i \end{bmatrix} = [\, R \quad T \,] \begin{bmatrix} X \\ Y \\ Z \\ 1 \end{bmatrix} \tag{2}$$

where R is a 3x3 orthogonal rotation matrix and T is a 3x1 translation vector. The components r_{ij} of the rotation matrix are composed of trigonometric relationships depending on which axis the camera is rotated. Then, the local coordinates (x_i, y_i, z_i) can be mapped into the 2D image coordinate system (x'_i, y'_i) from triangulation (Fig. 1) using

$$\begin{bmatrix} x'_i \\ y'_i \\ 1 \end{bmatrix} = \begin{bmatrix} f & 0 & 0 \\ 0 & f & 0 \\ 0 & 0 & 1 \end{bmatrix} \begin{bmatrix} x_i \\ y_i \\ z_i \end{bmatrix} \times \frac{1}{z_i} \tag{3}$$

Finally, the combination of both transformations is called the projective matrix "P", which maps the 3D point coordinates to 2D image coordinates using the camera pose.

$$P = \begin{bmatrix} f & 0 & 0 \\ 0 & f & 0 \\ 0 & 0 & 1 \end{bmatrix} \begin{bmatrix} r_{11} & r_{12} & r_{13} & x_t \\ r_{21} & r_{22} & r_{23} & y_t \\ r_{31} & r_{32} & r_{33} & z_t \end{bmatrix} \tag{4}$$

$$\begin{bmatrix} x'_i \\ y'_i \\ 1 \end{bmatrix} = P \times \begin{bmatrix} X \\ Y \\ Z \\ 1 \end{bmatrix} \tag{5}$$

The structure from motion problem turns into, given "n" fixed 3D points shared by "m" images, estimate "m" projection matrices P_i and "n" 3D points $S_j = [X_j \ Y_j \ Z_j \ 1]^T$ from the "mn" corresponding 2D points $s'_{ij} = [x'_{ij} \ y'_{ij} \ 1]^T$

$$s'_{ij} = P_i S_j, \qquad i = 1, ..., m, \qquad j = 1, ..., n \tag{6}$$

This formulation of the cost function for the structure from motion problem is a difficult non-convex optimization problem. Nevertheless, the epipolar constraint (Hartley and Zisserman 2004), derived from the computation of the epipolar plane's volume which is equal to zero, states:

$$s'^T_{1j}[T \times R] \, s'_{2j} = 0 \tag{6}$$

The epipolar constraint allows a more elegant solution (Eq. 6) to find the relative camera pose (R and T) independently of the 3D point coordinates. After the cameras pose and 3D coordinates are computed, a nonlinear refining method (bundle adjustment) is conducted to minimize the reprojection error (Fig. 2), which is the distance between the original location coordinates s' and the reprojected coordinates PS, projecting a previously back-projected 3D point onto the original camera. This process, applied to the built-up column experiments described in the next section, optimizes both 3D point location and camera viewing parameters simultaneously by minimizing the error

$$Error\ (P, S) = \sum_{i=1}^{m} \sum_{j=1}^{n} Distance\ (s'_{ij}, P_i S_j)^2 \tag{7}$$
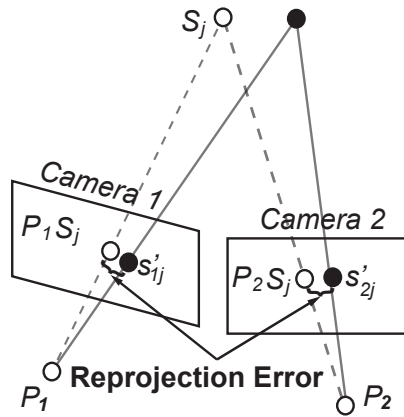

Figure 2. Reprojection error minimized by bundle adjustment

3. Experimental Program

3.1 Test procedures and setup

3D digital state models are created for six column tests that are part of a series of a built-up CFS column testing program at Johns Hopkins University through which studies on composite action, fastener spacing/layout, and column end conditions, as well as an extensive comparison to code-based predictions for strength are performed. The section studied is a back-to-back "I" section, with #10 sized self-drilling screws connecting the webs of 600S162-54 channel sections where the nominal out-to-out web width is 6 in [1.5 cm], flange width is 1.625 in [4.1 cm], lip length is 0.5 in [1.25 cm], and thickness is 0.0566 in [1.43 mm]. Fastener layouts are designed according to AISI S100-12 (2012) sections D1.2 and E4.2 for built-up columns. The code also requires prescriptive fastener end groupings, which are included in other tests that are part of a larger parametric study. The column tests reported here are fastened together with details described in the following sections.

The 600S162-54 lipped channel section is chosen for its local and distortional slenderness common for design. The column height is 3 ft [0.91 m], with enough length for at least one distortional buckling half wavelength of 14.5 in [36.8 cm] to develop. This half-wavelength is obtained from a signature curve analysis of a single section using finite-strip based elastic buckling software CUFSM (Schafer and Ádàny 2006). Local buckling is also expected from the various fastener layouts used in the tests.

Fig. 3 shows the MTS rig test setup. The tests were displacement-controlled with a load rate that does not exceed 0.03 in/min [0.76 mm/min]. The names of the trials (a subset of a larger parametric study) are A1a, A1b, A1c, A2, A3, A4; fastener spacings for each trial are illustrated in Fig. 4 and listed in Table 1.
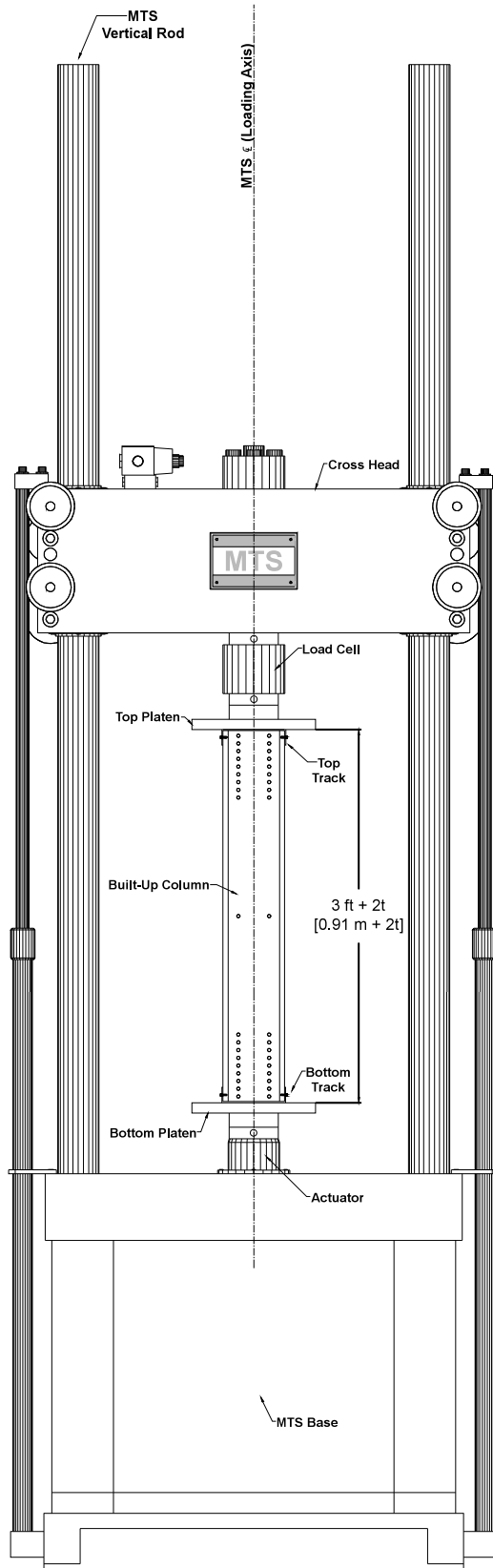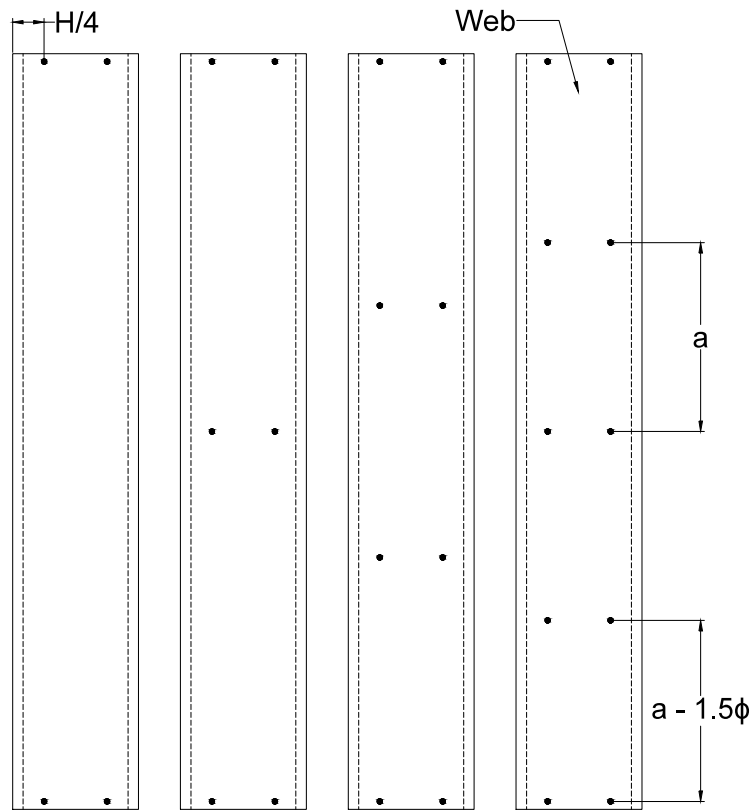
Figure 3. Elevation of MTS test rig setup

Figure 4. Fastener layout types tested, using (from left to right) L/1, L/2, L/3, and L/4 even fastener spacing *a*, where ϕ is the screw diameter

Table 1. Fastener layouts for trials

Trial	Fastener Layout	Spacing, a (in) [mm]*
A1a	*L*/1	36 [914]
A1b	*L*/1	36 [914]
A1c	*L*/1	36 [914]
A2	*L*/2	18 [457]
A3	*L*/3	12 [305]
A4	*L*/4	9.0 [229]

*Note: an offset of 1.5ϕ (or 0.375 in [9.5 mm]) from the ends of the columns must be applied to the top and bottom fastener pairs

3.2 Material testing

Coupon tests were performed on the 600S162-54 channel sections. Testing was completed in accordance with ASTM A370-12a (2012) and all test results are shown in Table 2. Yield (at 0.2% offset) and ultimate tensile strengths for the 600S162-54 sections were recorded with a mean of 57.4 ksi [396 MPa].

Table 2. Tensile coupon test results

Specimen	Base Metal Thickness t (in) [mm]	Gauge Elongation ΔL_g (%)	Yield Strength* $F_{y,0.2}$ (ksi) [MPa]	Upper Yield Strength $F_{y,up}$ (ksi) [MPa]	Tensile Strength F_u (ksi) [MPa]	Strain at Tensile Strength ε_u (in/in)
600S162-W1	0.055 [1.40]	24.40	57.8 [398]	57.8 [399]	69.7 [480]	0.178
600S162-W2	0.055 [1.39]	22.18	57.9 [399]	57.9 [399]	69.7 [481]	0.176
600S162-F1	0.054 [1.38]	21.68	57.2 [395]	57.7 [398]	69.5 [480]	0.164
600S162-F2	0.054 [1.38]	23.00	56.7 [391]	57.1 [394]	70.1 [483]	0.180
Mean	0.055 [1.39]		57.4 [396]	57.6 [397]	69.8 [481]	
C.o.V.	0.008 [0.195]		0.010 [0.068]	0.006 [0.044]	0.004 [0.024]	

*The 0.2% Offset Method was used

3.3 Cameras setup and 3D image-based reconstruction procedure

A set of 4 pairs of static cameras (Table 3) were located around the specimens covering a 360° view (Fig. 5). Before starting each test a set of 120 images were taken around the test setup to provide a digital state model containing the location and orientation of the static cameras. This procedure allowed the incorporation of all 8 static cameras in the 3D reconstruction process, eliminating the need for overlapping camera pose estimation which can be time consuming. The 8 static cameras took pictures at 6 frames/minute. For every 0.02 in [0.508 mm] axial column displacement increment a new detailed 3D point cloud was created with 120 images which was then aligned to the original digital model using the static cameras location and orientation. The digital state models were scaled using the test platen dimensions providing a mean accuracy of ±0.02 in [0.5 mm].

Table 3. Cameras and lenses

| Camera	Model	Lens ID	ISO	Shutter Speed (seconds)	Aperture	Image Resolution (megapixels)
C1	NIKON D7100	AF Nikkor 20mm f/2.8D	800	1/25	f/5	24
C2	NIKON D7100	AF Nikkor 20mm f/2.8D	800	1/25	f/5	24
C3	NIKON D7100	AF Nikkor 20mm f/2.8D	800	1/25	f/5	24
C4	NIKON D7100	AF Nikkor 20mm f/2.8D	800	1/25	f/5	24
C5	Canon EOS REBEL T3	EF-S18-55mm f/3.5-5.6 IS II	800	1/25	f/5.6	12
C6	Canon EOS REBEL T3	EF-S18-55mm f/3.5-5.6 IS II	800	1/25	f/5.6	12
C7	NIKON D7100	Zoom-Nikkor 18-55mm f/3.5-5.6G	1000	1/25	f/6.3	24
C8	NIKON D7100	Zoom-Nikkor 18-55mm f/3.5-5.6G	1000	1/25	f/6.3	24
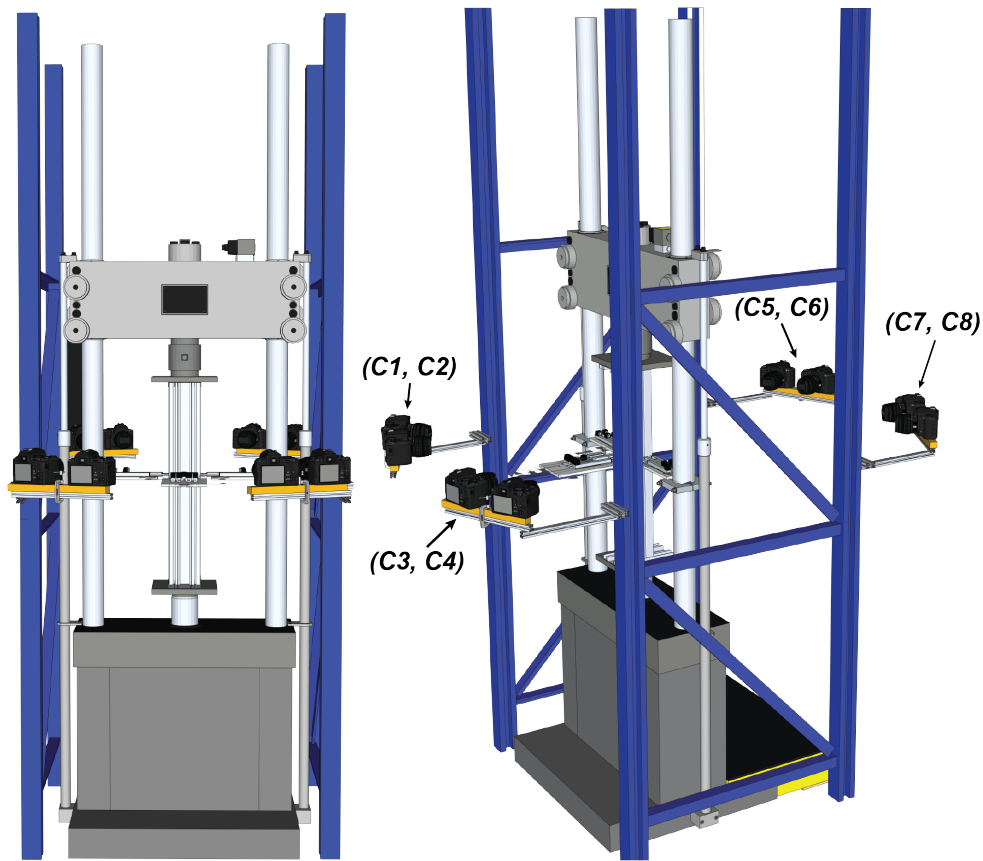
Figure 5. Camera setup

3.4 Test results summary

Test results are shown in Table 4. All 6 trials showed a consistent combined local and distortional buckling-controlled failure with similar peak capacities. The peak loads increased slightly as more web screws were introduced in the built-up columns. A composite buckling mode where both webs deformed in unison and with the same local buckling half-wavelength directions was only achieved in trial A4 with the tightest screw spacing of $L/4$. Fig. 6 shows that with a decrease in screw spacing (as with trials A2-A4), the position and length the buckling half-waves is influenced by the screw positions which can be quantitatively compared with the digital state models presented in the next section.

Table 4. Experimental results

Trial	Fastener Spacing	Buckling Mode	P_{test} (kips) [kN]	Failure Mode
A1	L/1	L[a]	31.7 [141]	L/D[a]
AVT1	L/1	L[a]	31.4 [140]	L/D[a]
AVT2	L/1	L[a]	31.4 [140]	L/D[a]
A2	L/2	L[a]	32.4 [144]	L[a]
A3	L/3	L[a]	31.4 [140]	L[a]
A4	L/4	L[b]	32.7 [145]	L[b]

[a]non-sympathetic buckling mode (generally symmetric about the minor axis)
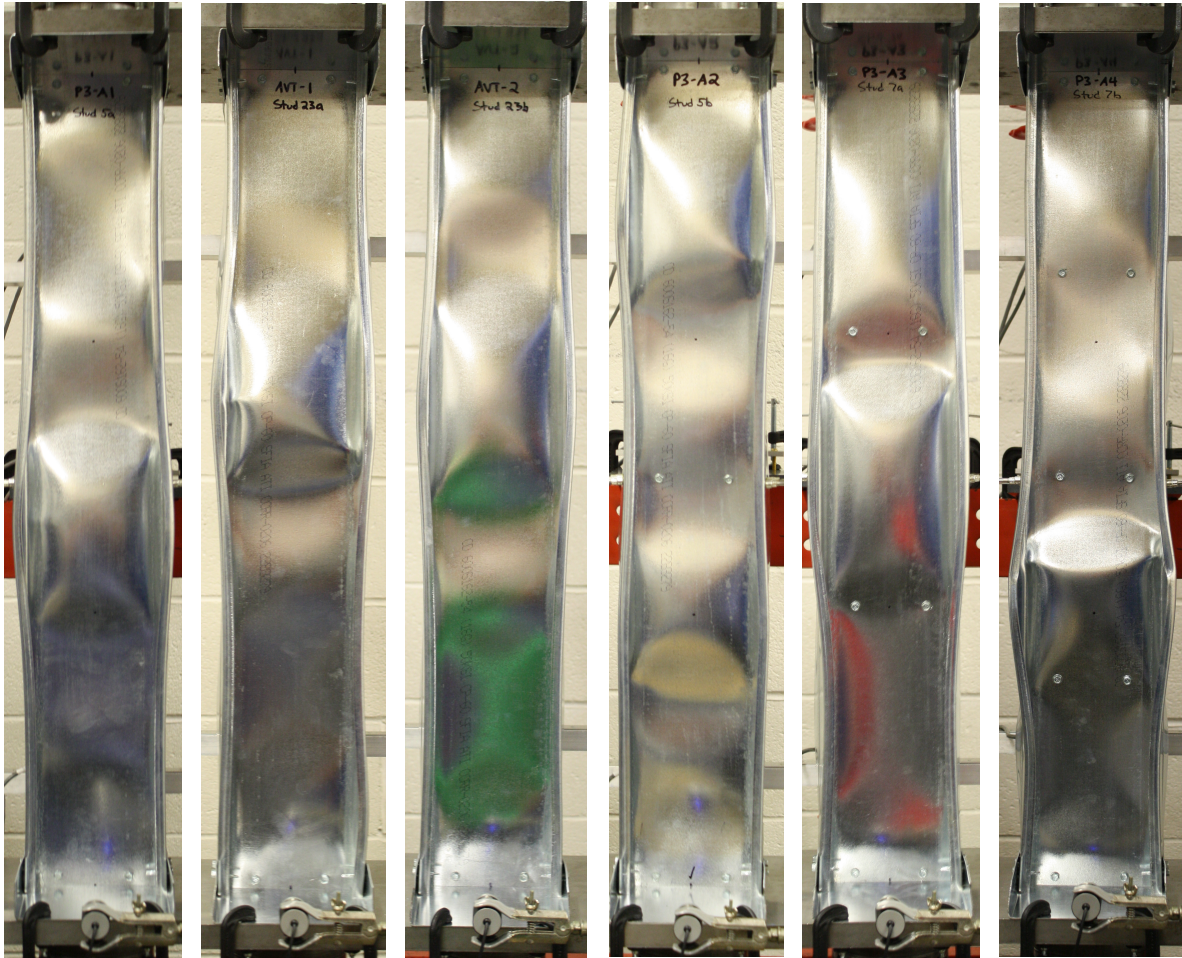[b]sympathetic buckling mode between the two studs (non-symmetric about minor axis)

Figure 6. Failure modes of tested specimens, with trials from left to right: A1a, A1b, A1c, A2, A3, and A4

4. Digital State Model Observations and Results
### 4.1 Permanent experimental record
The results from the digital state models provide detailed information of the testing environment, for example, the test setup typical point cloud in Fig. 7. Point clouds were reconstructed throughout testing for each specimen at a speed of one frame or digital state model every 10 seconds. This allows the researcher to go back at specific time steps and analyze the state of the specimen and test setup (e.g., take measurements, observe shape) and correlate with sensors data. Animated point clouds can also be used to produce visualizations from any angle and location.

Figure 7. 3D point cloud snapshot (using 37 million points)

4.2 State visualization and measurement

Digital state models can be used as visualization tools for the researcher. Fig. 8 show an undeformed isolated cold-formed steel stud element and a built-up member. These models can be incorporated into Portable Document Format (PDF) files for readers to interact (e.g., take measurements and visualize cross sections). Fig. 8 in the digital version of this paper can be rotated, zoomed, measured and many others type of manipulations.
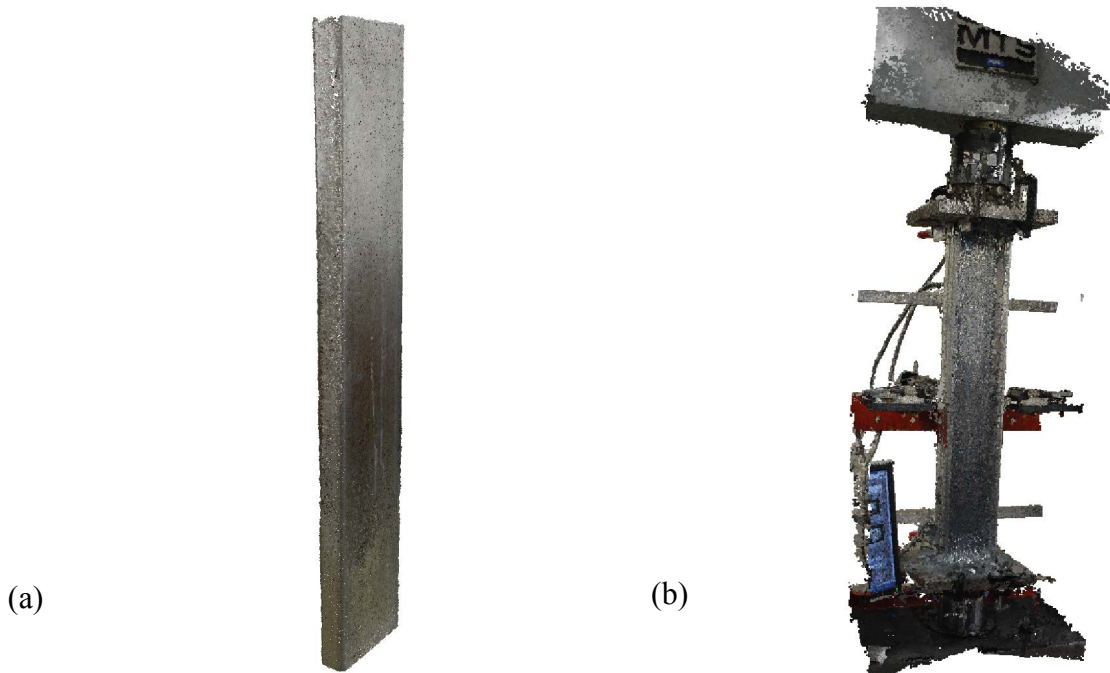
(a)   (b)

Figure 8. 3D point cloud: (a) an isolated cold-formed steel stud and (b) a built-up member

4.3 Initial geometric imperfections

Digital state models can also be used to compute initial geometric imperfections as shown in Fig. 9 for a single cold-formed steel stud created by using camera C1 with an AF Nikkor 20mm f/2.8D lens with an accuracy of ± 0.01 in [0.25 mm]. The member presents a variable cross-sectional angle of rotation (γ) and increasing horizontal deformation in the weak axis along the member.
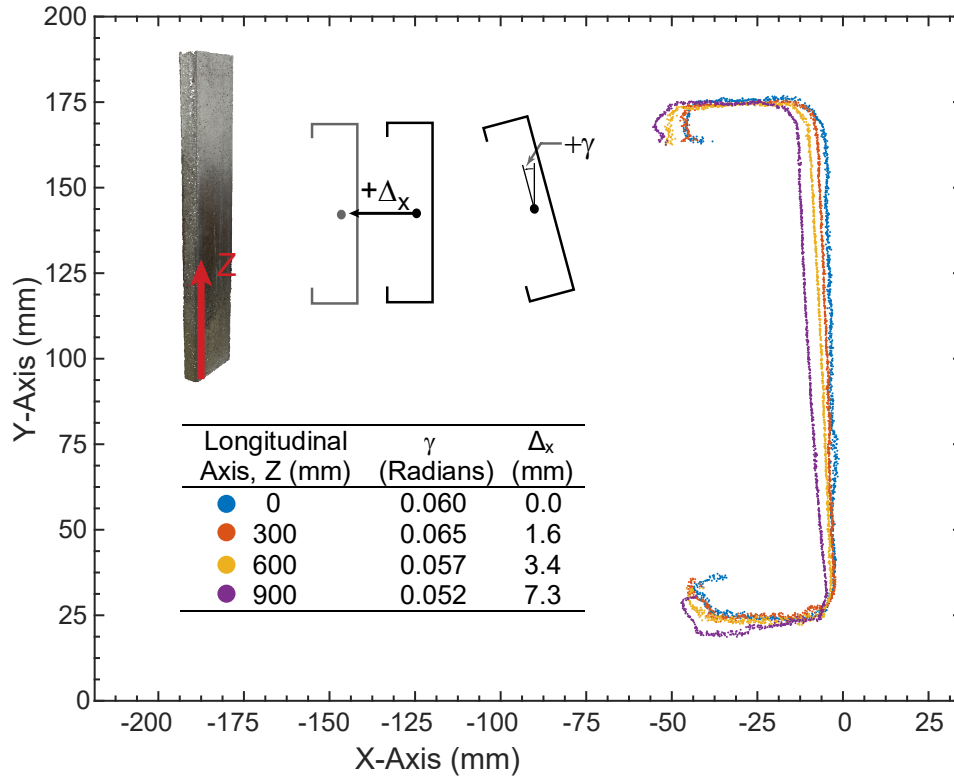

Longitudinal Axis, Z (mm)	γ (Radians)	Δ_x (mm)
0	0.060	0.0
300	0.065	1.6
600	0.057	3.4
900	0.052	7.3

Figure 9. Initial imperfection of a cold-formed steel stud

4.4 Specimen deformations and buckling half-wave documentation

A set of aligned and scaled digital state models can be also used to document buckling deformations fields by fitting a mesh on the point cloud and compute the variations in the nodes. Fig. 10 highlights this potential application where mid-web cross-section deformation for Specimen 1 is tracked and showing the half-waves deformation along the specimen. This sparsity and noisy cross sections, in comparison with Fig. 9, are because of the implementation of the Zoom-Nikkor 18-55mm f/3.5-5.6G lenses and the change in scene conditions.
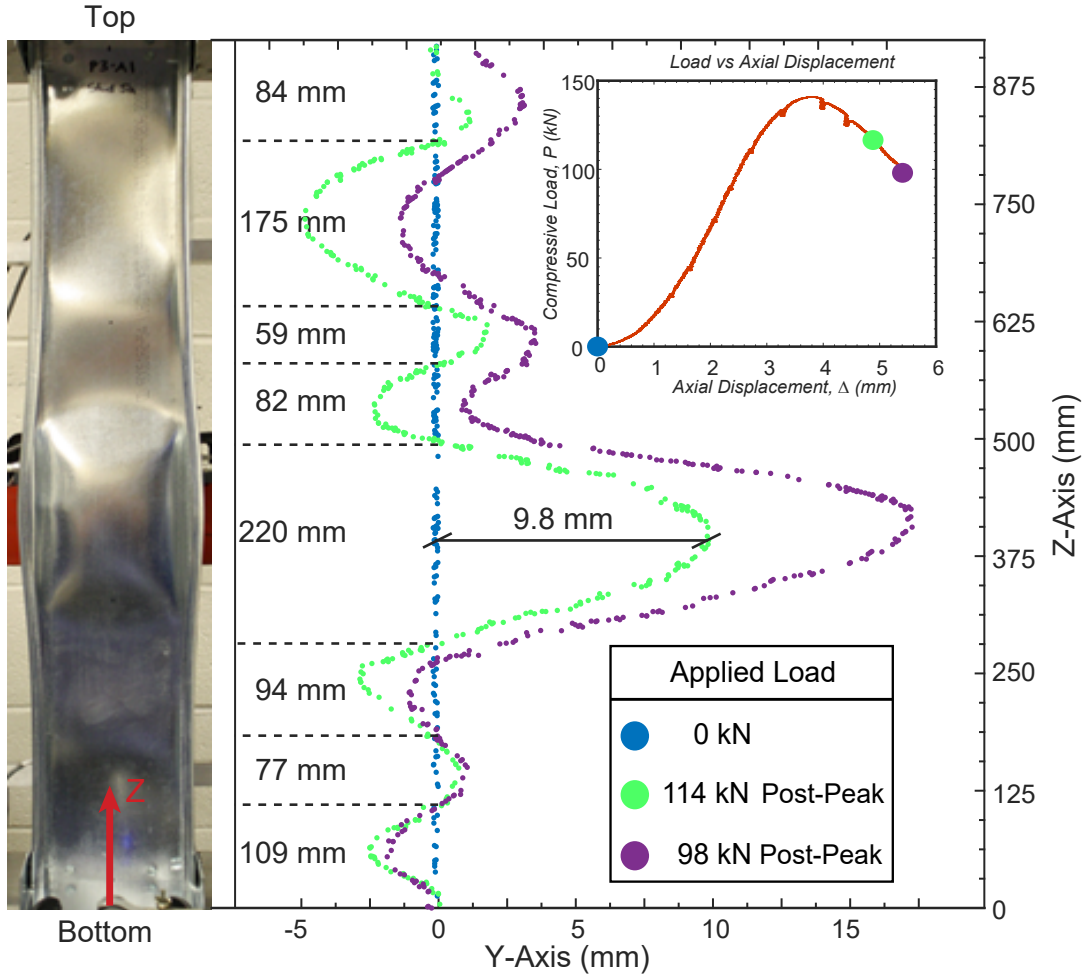
Figure 10. Specimen 1 cross-section deformation as function of axial load. Y-Axis is zoomed by a factor of 25 relative to Z-Axis

Fig. 10 illustrates the plate deformation at mid-web along the length, capturing the local buckling-induced deformation and failure at two loading steps after peak load was reached. After conducting an elastic buckling analysis in CUFSM (Schafer and Ádàny 2006), the local buckling half-wavelength for a single 600S162-54 section is 114 mm [4.5 in.], which can still be seen in the post-peak regime in the left-most ends of the scatter plots in Fig. 10. The other longer half-wavelengths developed (near column mid-height) in the post-peak regime and are a function of fastener spacing, degree of plastic hinge formation, buckling mode interactions, initial geometric imperfections, and whether or not the webs buckled in a sympathetic mode.

In order to further analyze the effect of fastener spacing, the reconstructed data in Fig. 11 can be used to show the plate buckling behavior of the web of the front stud of the built-up column, for all 4 fastener spacings studied. In the L/1 case, the webs of the two studs are not well-connected along the column height, and a large local buckling half-wavelength of approximately 225 mm [8.86 in.] develops in the post-buckling regime. With further connectivity between the webs, a sympathetic mode develops in case L/4 with a tighter fastener spacing of 9 in. [mm], but also several local buckling half-wavelengths decrease to 90 mm [3.54 in.], which are less than the elastic local buckling half-wavelengths recorded from CUFSM.
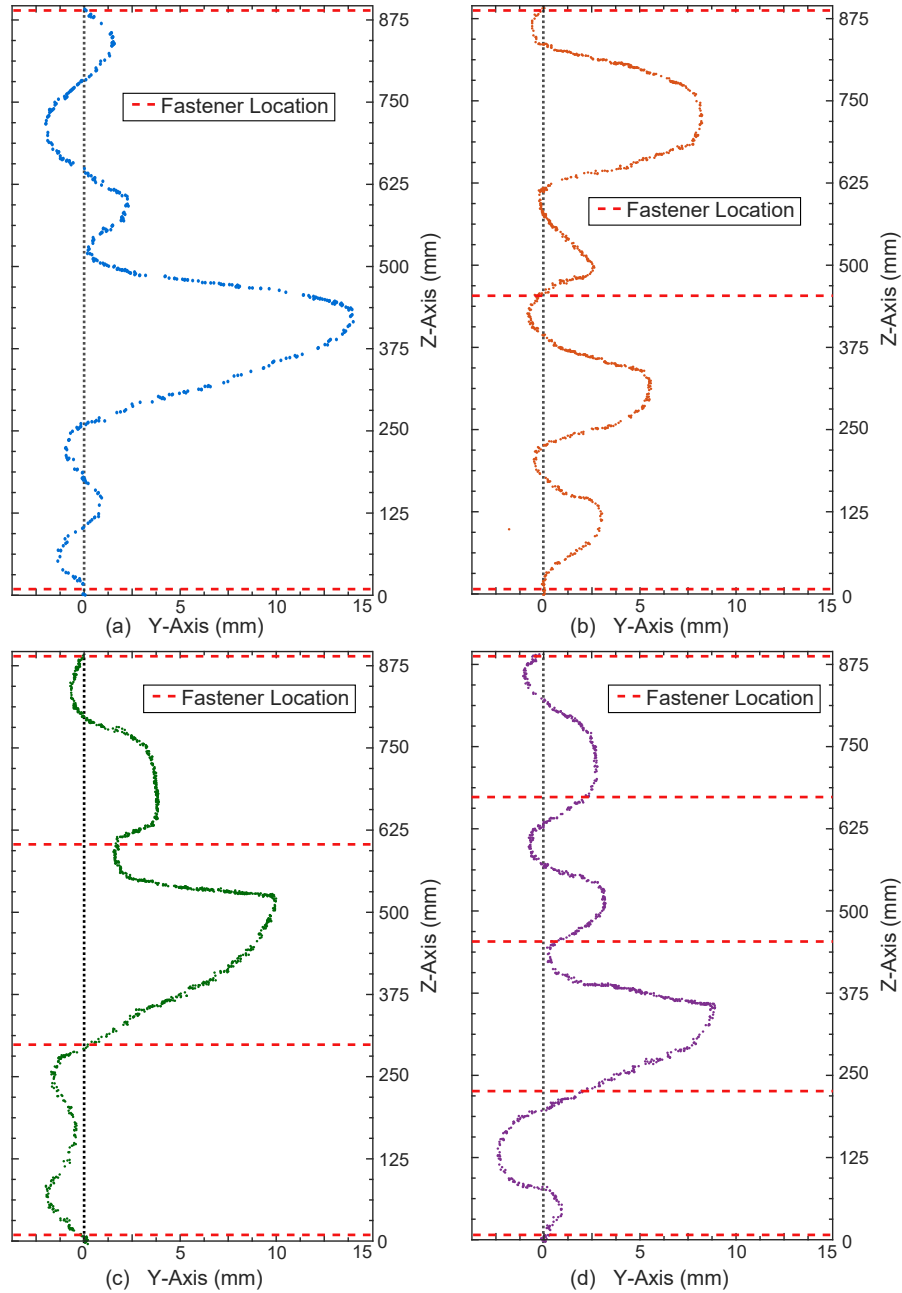
Figure 11. Specimens cross-section deformation as function of fasteners layout for (a) A1, (b) A2, (c) A3, and (d) A4. Y-Axes are zoomed by a factor of 25 relative to Z-Axes

5. Conclusions

Off-the-shelf digital single lens cameras and software were implemented to reconstruct 3D digital state models, every 10 seconds, of six built-up cold-formed steel columns from initial loading to collapse to the post-buckling response. Each image reconstruction were composed of approximately 30 million points, when using 120 images, and 11 million when using 8. Digital models provide a tool to measure initial geometric imperfections (for the specimen only and also for the specimen once installed in the test setup), track fastener deformations, and document buckling half-waves as they develop elastically.

Deformations beyond elastic buckling can also be tracked and compared with actual test measurements at peak and post-peak loads. Digital state models offer data that opens the field for new algorithms to be developed, such as buckling mode decomposition. Point clouds serve as a visualization tool that can be embedded into PDF files which allows the reader to interact with the model taking measurements or cross sections. The digital state models allow full field buckling deformation measurement along the column lengths revealing in this study that local buckling half-wave location and half-wavelength are influenced by fastener patterns.

Acknowledgements

References

AISC 360 (2010). *Specification for Structural Steel Buildings*, American Institute of Steel Construction, Chicago, IL.

AISI-S100.(2012). *North American Specification for the Design of Cold-Formed Steel Structural Members*, American Iron and Steel Institute, Washington, D.C.

American Society for Testing and Materials (ASTM), Standard Test Methods and Definitions for Mechanical Testing of Steel Products (ASTM370-12a), ASTM, West Conshohocken, PA, 2012.

Bellocchio, F. (2013). "3D surface reconstruction: multi-scale hierarchical approaches". Springer, New York.

Blostein, D., and Ahuja, N. (1989). "Shape from texture: integrating texture-element extraction and surface estimation". *IEEE Transactions on Pattern Analysis and Machine Intelligence*, 11, 1233-1251.

Didden, E.-M., Thorarinsdottir, T. L., Lenkoski, A., & Schnorr, C. (2015). "Shape from Texture Using Locally Scaled Point Processes". *Image Analysis & Stereology*, 34(3), 161–170.

Favaro, P., & Soatto, S. (2005). "A geometric approach to shape from defocus". *IEEE Transactions on Pattern Analysis and Machine Intelligence*, 27(3), 406–417.

Fratamico, D.C. and Schafer, B.W. (2014). "Numerical Studies on the Composite Action and Buckling Behavior of Built-Up Cold-Formed Steel Columns." *22nd International Specialty Conference on Cold-Formed Steel Structures*, St. Louis, MO.

Fratamico, D.C., Torabian, S., Schafer, B.W. (2015). "Composite Action in Global Buckling of Built-Up Columns Using Semi-Analytical Fastener Elements." Proceedings of the Annual Stability Conference, Structural Stability Research Council, Nashville, TN.

Georgieva, I., Schueremans, L., Pyl, L., Vandewalle, L. (2012). "Experimental investigation of built-up double-Z members in bending and compression." *Thin-Walled Structures*, 53, 48-57.

Golparvar-Fard, M., Peña-Mora, F., Arboleda, C., and Lee, S. (2009). "Visualization of Construction Progress Monitoring with 4D Simulation Model Overlaid on Time-Lapsed Photographs." *J. Comput. Civ. Eng.* 23, SPECIAL ISSUE: Graphical 3D Visualization in Architecture, Engineering, and Construction, 391–404.

Hartley, R., Zisserman, A. (2004). "Multiple view geometry in computer vision". Cambridge University Press, New York.

Lama Salomon, A., Tao, F., Cai, J., Moen, C. D. (2015). "Buckling mode identification for a cold-formed steel column experiment with 3D image-based reconstruction" Proceedings of the Annual Stability Conference, Structural Stability Research Council, Nashville, TN.

Lama Salomon, A., Sprinkel, M., Moen, C.D. (2016). "Bridge Deck Cracking Structural Investigation With Computer Vision-informed Infrastructure Condition Assessment." Proceedings of the Annual Transportation Research Board Conference, Washington, D.C.

Lattanzi, D., and Miller, G. R. (2015). "3D Scene Reconstruction for Robotic Bridge Inspection". *Journal of Infrastructure Systems*, 21.

Maia, W.F. et al. (2012). "Numerical and Experimental Investigation of Cold-Formed Steel Double Angle Members Under Compression." *21st International Specialty Conference on Cold-Formed Steel Structures*, St. Louis, MO.

MATLAB 2015b, The MathWorks, Inc., Natick, MA, United States.

Potmesil, M. (1987). "Generating octree models of 3D objects from their silhouettes in a sequence of images". *Computer Vision, Graphics, and Image Processing*, 40, 1–29

Schafer, B.W. and Ádàny, S. (2006). "Buckling analysis of cold-formed steel members using CUFSM: conventional and constrained finite strip methods." *18th International Specialty Conference on Cold-Formed Steel Structures*, Orlando, FL.

Stone, T.A. and LaBoube, R.A. (2005). "Behavior of cold-formed steel built-up I-sections." *Thin-Walled Structures*, 43(12), 1805-1817.

Torresani, L., Hertzmann, A., & Bregler, C. (2008). Nonrigid Structure-from-Motion: Estimating Shape and Motion with Hierarchical Priors. IEEE Transactions on Pattern Analysis and Machine Intelligence, 30(5), 878–892.

Wu, C. (2011). "VisualSFM: A Visual Structure from Motion System – Documentation". <http://ccwu.me/vsfm/> accessed February 28, 2014.

Wu, C. (2013). "Towards Linear-Time Incremental Structure from Motion." 2013 International Conference on 3DV-Conference, 127–134.

Zhao, X., Tootkaboni, M., Schafer, B.W. (2015). "Development of a Laser-Based Geometric Imperfection Measurement Platform with Application to Cold-Formed Steel Construction." *Experimental Mechanics*, 55, 1779-1790.